Available online at www.sciencedirect.com
ScienceDirect
Journal of Structural Biology 158 (2007) 233–243
Journal of Structural Biology
www.elsevier.com/locate/yjsbi

High-throughput screening of cellular features using high-resolution light-microscopy; Application for profiling drug effects on cell adhesion

Yael Paran [a], Micha Ilan [b], Yoel Kashman [c], Sofee Goldstein [c], Yuvalal Liron [a], Benjamin Geiger [a], Zvi Kam [a,*]

[a] *Department of Molecular Cell Biology, Weizmann Institute of Science, Rehovot 76100, Israel*
[b] *HTS Center, Department of Zoology, Tel Aviv University, Tel Aviv 69978, Israel*
[c] *School of Chemistry, Tel Aviv University, Tel Aviv 69978, Israel*

Received 10 April 2006; received in revised form 29 August 2006; accepted 18 December 2006
Available online 17 January 2007

Abstract

High-resolution light-microscopy and high-throughput screening are two essential methodologies for characterizing cellular phenotypes. Optimally combining these methodologies in cell-based screening to test detailed molecular and cellular responses to multiple perturbations constitutes a major challenge. Here we describe the development and application of a screening microscope platform that automatically acquires and interprets sub-micron resolution images at fast rates. The analysis pipeline is based on the quantification of multiple subcellular features and statistical comparisons of their distributions in treated vs. control cells. Using this platform, we screened 2200 natural extracts for their effects on the fine structure and organization of focal adhesions. This screen identified 15 effective extracts whose fractionation and characterization were further analyzed using the same microscope system. The significance of combining resolution, throughput and multi-parametric analyses for biomedical research and drug discovery is discussed.
© 2007 Elsevier Inc. All rights reserved.

Keywords: Cell-based screening; High-resolution light-microscopy; Image analysis; Natural compounds; Focal adhesion

1. Introduction

Cell-based screening is an emerging methodology for exploring cellular processes and their modulation by chemical or genetic perturbations. Use of the intact live cell as a reporter enables a multi-parametric characterization of responses to such perturbations, affecting a variety of molecular and cellular targets, as well as responses of the interconnected normal or diseased cellular-pathway networks, while taking into account accessibility to subcellular compartments, cell-type specificity, biostability, toxicity and adverse side effects (Abraham et al., 2004; Butcher, 2005; Clemons, 2004).

Cell-based screening challenges multiple aspects of experimental biology, including the preparation of suitable reporter cells, automated microscope readouts for high-throughput screening of large libraries, and the development of algorithms for image analysis and interpretation linked to high-level bioinformatics databases. These considerations have motivated the development of high-content screening methods based on microscopy of reporter cells, engineered to show the activity or organization of molecular targets inside living cells (Abraham et al., 2004; Giuliano et al., 2003; Liebel et al., 2003; Mitchison, 2005; Peterson and Mitchison, 2002; Smith and Eisenstein, 2005; Tanaka et al., 2005; Yarrow et al., 2003), including cell-cycle phases (Perlman et al., 2005; Zhou et al., 2006), overall cellular and cytoskeletal morphology (Mitchison, 2005; Tanaka et al., 2005), and cell fate (Arrasate and Finkbeiner, 2005). However, most of the existing screening

* Corresponding author. Fax: +972 8 9344125.
E-mail address: zvi.kam@weizmann.ac.il (Z. Kam).

1047-8477/$ - see front matter © 2007 Elsevier Inc. All rights reserved.
doi:10.1016/j.jsb.2006.12.013

microscopes represent a compromise between high-content and high-throughput performance, and are thus limited in their capacity to provide detailed information on fine cellular features in large screens.

Another challenge for cell-based screening is the computerized evaluation of the acquired images. Algorithms have been developed for the analysis of textural and morphological parameters, based on machine learning (Conrad et al., 2004; Hu and Murphy, 2004; Murphy, 2004; Zhao et al., 2005), segmentation approaches and statistical methods (Conrad et al., 2004; Perlman et al., 2005; Perlman et al., 2004; Tanaka et al., 2005). Their application in the analysis of high-throughput experiments enables linking the images acquired in screens to specific biological phenotypes.

In this work, we describe the development of a screening light-microscope for high-throughput and high-resolution (HTR) imaging and analysis of cell samples. The HTR system acquires 3×10^3 images per hour at a pixel resolution of 0.3 μm, taking 16–25 images in each well to maintain cell-level statistics of low magnification imaging. To match the throughput of image processing and interpretation to that of the acquisition, we developed an automated unsupervised multi-parametric analysis pipeline, designed to quantify subcellular details.

We used the HTR platform to screen a natural-products library for compounds affecting cell-matrix adhesion structures. Such libraries have been shown to be rich sources for biologically active molecules (Koehn and Carter, 2005). Focal adhesions (FA) to the matrix, and the related focal complexes, examined here, are small (less than one, to several μm^2) multi-protein complexes that connect matrix molecules to the actin cytoskeleton. They play a central role in a variety of cellular processes, including tissue morphogenesis, cytoskeletal organization and cell migration. FA characteristics, including their prominence, size, shape, molecular composition and spatial distribution, provide valuable information on cell structure, dynamics and function. The HTR screen described here and the automated analysis of the acquired images provide detailed information on the effects of candidate drugs on FA morphology and the associated cytoskeleton.

2. Methods

2.1. Extracts library

The natural-extracts library screened here consisted of 2200 extracts collected at the National Center for High Throughput Screening of Novel Bioactive Compounds (NCHTS) of Tel Aviv University, Israel (http://www.tau.ac.il/~nchts). The extracts were derived mainly from marine and terrestrial microorganisms, plants and animals. Freshly collected samples were freeze-dried and extracted with ethyl acetate (3×), followed by ethyl acetate/MeOH 1:1 (3×). The combined organic phase was evaporated and the dry material was dissolved with dimethyl sulfoxide (DMSO) to a concentration of 10 mg/ml. Extracts were kept in 96-well formats, and blindly supplied to the screening step, coded only by plate and well annotations. They were applied to the cell cultured in multi-well plates at two concentrations (see below).

Further fractionation steps were applied to extracts found by this screen, including separation according to solvent polarity (using aqueous methanol and hexane, chloroform or ethyl acetate), followed by chromatography on Sephadex LH-20 and HPLC columns and collection of multiple fractions. Each fraction was then applied at 5–11 concentrations to the multi-well cultures, and screened using the HTS system. Active fractions were subjected to further purification.

2.2. Purification of jaspamide

Dry sponge (10 g) was extracted with ethyl acetate (3×). The combined organic phase was evaporated to afford a brown gum (120 mg). The gum was chromatographed on a Sephadex LH-20 column, eluted with methanol, and the active fraction containing ca. 80% jaspamide was further purified by HPLC, RP-18 column and eluted with methanol/water to give 3 mg of pure jaspamide, according to its 1D and 2D NMR and MS spectra.

2.3. Reporter cells

A rat embryonic fibroblast line (REF52) was retrovirally infected with yellow fluorescence protein (YFP)-tagged human paxillin in pBabe vector (Dr. I. Lavelin, Weizmann Institute of Science, Israel, unpublished data). Single-cell cloning was used to obtain a morphologically uniform population. Labeling for actin and paxillin by immunostaining demonstrated that FA and actin cytoskeleton organization in the cloned cells was indistinguishable from that of the parental REF52 cells (data not shown). The paxillin-tagged clone was used to highlight FA in control and treated samples.

2.4. Screening protocol

REF52 reporter cells were suspended in 50 μl Dulbeco's modified Eagle's medium (DMEM; Invitrogen Co.) + 10% fetal calf serum (FCS; Biological Industries, Beit-Haemek, Israel), seeded at a density of 800 cells per well in 384-well assay plates (Greiner bio-one GmbH, Fricjkenhausen, Germany; F-bottom, μClear, black, tissue-culture-treated), and cultured for 24 h at 37 °C with 5% CO_2. The extracts dissolved in DMSO were diluted 1:10 in DMEM and then 1:100 and 1:1000 in DMEM + 10% FCS to give final extract concentrations of 100 and 10 μg/ml, respectively. In each 384-well plate, 88 extracts were tested at both concentrations by replacing the cell medium with the diluted extracts and incubating for 90 min. At the end of the treatment, the cells were fixed by dipping the whole plate in 3% paraformaldehyde (PFA) for 20 min and then washing

with PBS. Control wells were supplied with DMEM + 10% FCS or with DMEM + 10% FCS + 1% DMSO. The plates with fixed cells in PBS were sealed with parafilm and placed on the microscope stage for screening.

Selected extracts that were found effective were fractionated and the fractions were screened in multi-well plates at 5–11 dilutions (from 10^{-1} to 10^{-11} mg/ml), in duplicates, using the HTR system (Fig. 1a and supplementary Fig. 1 online). The purified compounds were further studied to establish concentration and time dependence of the cellular responses.

2.5. Microscope and controlling program

The automatic microscope systems (Paran et al., 2006) are based on IX71 and IX81 microscopes (Olympus, Tokyo, Japan). Automation is provided by ProScan (Prior, Cambridge, UK), including XY stage, focus, shutters, and excitation and emission filter wheels. A fast laser Auto-Focus attachment (Liron et al., 2006) was applied to adjust the objective to focus before each image was acquired. The CCD camera is a Quantix 57 (Photometrics, Tucson, AZ). The system is controlled by Resolve6D software running in the RedHat Linux operating system. UCSF Image Visualization Environment (http://msg.ucsf.edu/IVE) and Priism libraries are used for image display and graphic user interfaces (GUIs). The acquired images in each well are tiled into montages to enable an overall visual impression that eye-averages cell variability and detects consistent effects. Mouse-clicking on a well in a plate graphic interface (Plate GUI) allows seeing the montage image corresponding to this well. Clicking on an individual field within each well (Well GUI) or on a tile in the montage displays the full-resolution image (Fig. 1b), conveniently linking images to treatments/drugs for interactive display, or for monitoring the results of the automated analysis.

2.6. Image analysis

The general design of our computerized image analysis is shown schematically in Fig. 1c. Images were first segmented into objects, using WaterShed algorithm (Zamir et al., 1999) or binary thresholding of the high-pass filtered images. For each object, morphological, fluorescence-intensity and background estimated parameters were calculated (Table 1). In addition, percent area covered by cells ("cell coverage") was calculated for each image using the difference between the cell-free background level and cytoplasm diffuse fluorescence. This allowed clear identification of toxic effects and cell death, as well as quantitative normalization for cell adhesion objects per cell area. Object-by-object multi-parameter data was saved for each image in a separate file. User-controlled ranges for each parameter (minimum, maximum, gates) defined the allowable objects, excluded outliers and set non-parametric statistical parameters for the distributions. Evaluation of the variation in parameters of the segmented objects following treatment was then conducted by non-parametric statistical comparison tests applied for each treated well against all control wells. This evaluation yielded scores describing the changes between the treated and control wells.

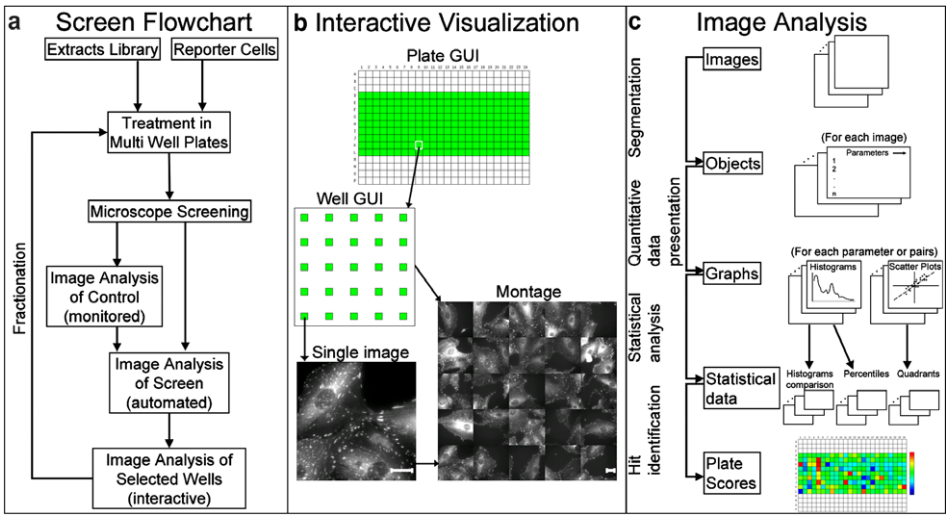

Fig. 1. Flowchart of the screen, image visualization and analysis. (a) Screen. Reporter cells are treated by the extracts library in multi-well plates, and images are acquired by automated microscopy. The parameter ranges and gates for the analysis are first defined manually for controls, and then applied for the whole screen. Wells depicted by this analysis for strong effects are further characterized, extracts fractionated, and cycles of purifications and repeated screens are applied to identify the active pure compound. (b) Visualization. A mouse-click on a well icon in the graphic user interface (Plate GUI) activates a view of the montage of images acquired in this well. Full-resolution images are displayed by mouse-clicking on the corresponding image icon in the Well GUI. Scale bar: 20 μm. (c) Image analysis. Image segmentation defines objects (i.e., individual FA). Object-by-object morphological and fluorescence intensity parameters are saved for every image. Statistical tests compare the accumulated distributions of each parameter for all control wells with those in each treated well, yielding scores for all wells and every parameter. These scores are displayed by the Plate GUI in color codes, and are used to rank the wells for visualization (ordered by scored effects) and for further characterization.

Table 1
Morphological and fluorescence parameters for each segmented object

	Parameter	Description
General	Flag	Object number Negative value flags to exclude object due to selective criteria
Global image parameters	CA	Cell area (for the cell that contains the object) or cell coverage in the image
	$C_{x,yz}$	Cell center coordinates
	$E_{x,y}$(k)	Cell edge outline polygon
	N	Number of objects in cell/image
Morphological parameters for each object	$cm_{x,y,z}$	Center of mass coordinates (fluorescent intensity weighted)
	A	Area
	P	Perimeter
	SF	Shape factor $= P/\mathrm{sqrt}(4\pi A)$
	L_m, L_n	Long and short axes of best fitted ellipsoid
	SM	Smooth factor $= A/(\pi L_m L_n)$
	Ang	Angle of long axis
	Rang	Relative angle to direction of cell center
	Axrt	Axial ratio $= L_m/L_n$
	R_g	Radius of gyration
	CH_A, CH_P	Convex hull area and perimeter
	Solidity	A/CH_A
	Roughness	P/CH_P
	X_{min}, X_{max}, Y_{min}, Y_{max}	Rectangular extent
	D_c	Distance to cell center
	D_p	Shortest distance to cell edge
	NDE	Normalized distance between cell edge and cell center $= D_p/(D_p+D_c)$
Parameters for cytoskeleton morphology	I_F	Fiber-associated total intensity
	L_F	Total fibers length
	I/L	Intensity per unit length
Fluorescence intensities for each object	T_i	Total (integrated) fluorescent intensity for each labeled color ($i = 1, 5$)
	B_i	Local background intensity
	F_i	Background subtracted total intensity
	Txt_j	Texture parameters

Combining scores for each parameter yielded multiple-parameter ranking of scores and ordering of the respective wells. This order was based on the best score for the selected parameters (showing wells in which at least one of the analysis parameters was strongly affected), on the average score, or on the worst score (depicting wells in which all of the selected parameters showed strong effects). This procedure allowed us to view wells ordered according to their degree of deviation from controls, and to judge visually how many of the top selected wells should be considered for further inspection.

2.7. Statistics

An accumulated histogram for each tested parameter was normalized and compared to the respective accumulated histogram for the objects combined from all control wells. Wilcoxon Rank-Sum (WR) (Brownlee, 1965) and Kolmogorov–Smirnov (KS) (Press et al., 1986) tests comparing two sampled lists were adapted to compare histograms. Since null hypothesis probabilities require statistical models, which are difficult to establish here, we used ad-hoc scores, inspired by WR and KS, to estimate differences between histograms (see Supplementary methods online). The approach was based on calculating the sum of the absolute differences between channels of the normalized histograms (KSsa). In addition, we applied two more non-parametric statistical measures: (i) the 90th percentile value for a single parameter to estimate the shift in that parameter's distribution (ii) a two-parameter quadrant evaluating simultaneous alterations in two parameters' distributions, using the 90th percentile value of each parameter in control wells as the gate values. The score was defined as the fraction of objects in each quadrant out of the total number of objects in the tested sample.

2.8. Visualization of plate scores

Plate summary of the scores (plate scores) are displayed in spectral-color code. The color scale was set by the mean and standard deviation of the scores for the individual control well when compared to the accumulated data from all the control wells. The mean value of these scores determined the center (green) of the color scale, while their standard deviation indicated the range (red to blue). This color scale presented the variability in the untreated wells, but in order to display the effects of treatment the center and range of colors can be rescaled by the user.

3. Results

3.1. The screening process

The screen of a natural-extracts library for compounds affecting cell adhesion and the cytoskeleton was conducted on REF52 reporter cells expressing YFP-paxillin. Paxillin is a scaffold protein, associated with the FA submembrane complex (Brown and Turner, 2004). Extracts were added to the cells in 384-well plates (Fig. 1a) at two concentrations (100 and 10 μg/ml), and at least 24 wells in each plate were used as controls, treated with 1% DMSO alone. Following 90 min of incubation, the plates were fixed and screened with the HTR microscope using a 60×/0.9 numerical aperture (NA) objective.

For interactive inspection, we developed image-visualization tools to display single high-resolution images, as well as montages of multiple images called up by their well positions (Fig. 1b). To identify extracts that perturb normal FA morphology, the control cells were first characterized using quantitative WaterShed object segmentation and multi-parametric quantification (Zamir et al., 1999), followed by interactive selection of the optimal parameters to be used for the automated unsupervised analysis. For each parameter, we selected ranges and gates that define extreme effects, yet exclude outliers. All of the screened images were then automatically segmented and analyzed to "flag" the affected wells by comparing parameter distributions to the controls (Fig. 1c). The "flagged" images were then inspected visually, and interactive quantitative analysis was applied to further characterize the effects. The following sections describe these steps in detail.

3.2. Quantitative analysis of FA in control cells

To obtain quantitative information about FA structure, we have first determined the optimal optical setup of the microscope, by examining REF52 cells, expressing YFP-paxillin using different "dry" objective lenses, ranging from 10×/0.4 to 60×/0.9. To compare structural details observed with the different objectives, we brought all these images to the same magnification and examined them side by side. In Fig. 2a and b, we show overview images, taken with 20×/0.7 and 60×/0.9 objectives, respectively. The single 20× image (Fig. 2a) and the 3x3 image montage, taken with the 60× objective (Fig. 2b) show exactly the same area and the appearance of FA in them (at low resolution) is comparable. However, comparing the images at their maximal resolution reveals major differences in the apparent FA morphology observed using the different objectives, with many features detectable only at the highest magnification (Fig. 2c–f). Many near-by focal adhesions well resolved with the 60×/0.9 objective are merged into one blur with lower resolution objectives. The small focal complexes and fibrillar adhesions that are important indicators of the actin cytoskeleton activity and assembly states are mostly below detection level even with 40× objective. We

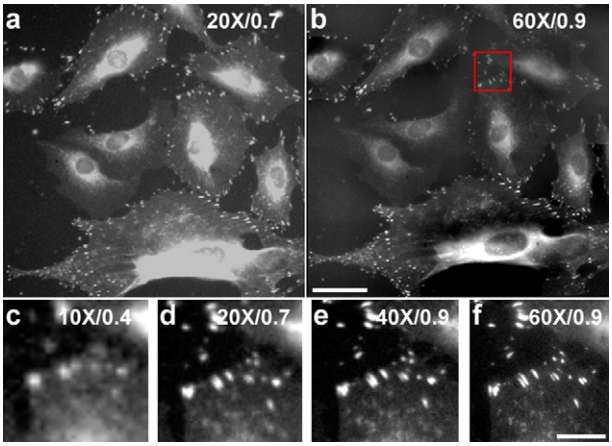

Fig. 2. Comparison of the optical magnification on focal adhesion detection. (a) Image of REF52 cells expressing YFP-paxillin obtained using 20×/0.7 objective. (b) Montage of 3 by 3 images obtained using 60×/0.9 objective of the same field of view as in (a). The images are not presented at their maximal resolution to allow comparison to (a). The red square shows the area enlarged in (c–f). Scale bar 50 μm. (c–f) The area marked in red square in (b) enlarged to maximal resolution obtained at 10×/0.4, 20×/0.7, 40×/0.9 and 60×/0.9 objectives, respectively. Scale bar 10 μm.

further tested the effect of the objective on the ability to resolve morphological changes in FA following treatment and found that at magnifications lower then 60× quantitative evaluation of FA size and shape were not reliable (see Supplementary Fig. 2 online). In view of these differences, all the screens were performed using the 60×/0.9 objective.

The morphological and intensity parameters of FA in untreated cells were quantified by analyzing control images following WaterShed image segmentation (Zamir et al., 1999). This segmentation defines FA as "objects", based on their fluorescence intensity and size range. The procedure calculates and exports morphological and signal-intensity parameters of each object (Table 1). By studying FA properties in control cells, we found three parameters that characterize FA-feature distributions: size (segmented object area), elongation (axial ratio for second-order best-ellipse fit) and mean fluorescence-signal intensity (indicating the amount of labeled protein). These parameters describe most small adhesion structures well, even though large ones may benefit from further characterization of internal protein distribution, texture and other features of shape complexity. The distributions of each of the aforementioned parameters in normal, untreated reporter cells were plotted as histograms (Fig. 3a), showing the wide distributions within the set ranges. The use of normally distributed statistical parameters to characterize and compare these histograms is clearly inapplicable. We therefore based comparisons of treated to control wells on non-parametric statistical tests and measures (see further on).

To optimize the sensitivity of the statistical tests for identifying responses to treatments, we determined acceptable ranges in FA of control cells for each parameter, so

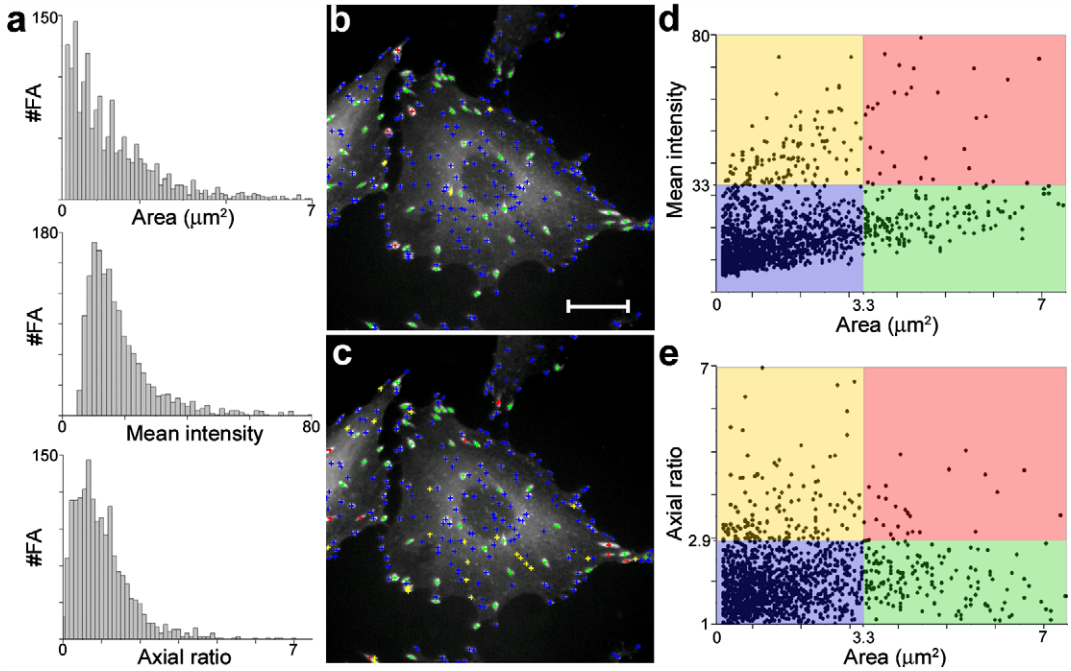

Fig. 3. Focal Adhesion (FA) segmentation and characterization. (a) Histograms of FA area, mean intensity and axial ratio, accumulated from 10 control cells, demonstrating the distributions of these parameters. (b) A typical reporter cell segmented, to define FA objects and calculate their parameters. The centers of mass of the FA are marked by crosses, color-coded according to parameter-pair quadrants of mean intensity vs. area. Scale bar: 20 μm. (c) Same as (b) scored for axial ratio vs. area. (d) Scatter plot of FA mean intensity vs. area from 10 control cells. The quadrants are defined by 90th percentile gate for each of the parameters. These quadrants are used to color-code the FA in (b). (e) Same as (d) for axial ratio vs. area. These quadrants are used to color-code the FA in (c).

that artifacts (such as perinuclear background staining or membrane protrusions) would be excluded (outliers). We also defined gates (using, e.g., 90th percentile values) that allow one- and two-parameter (quadrant) scores to depict changes in FA distribution tails (extremes). The power of such gating is well known from cell-sorter data analysis. Segmented FA in a typical reporter cell are shown in Fig. 3b and c, marked by a cross at their centers of mass. To identify FA with different properties, we colored the crosses according to the combination of two parameters, using gates to divide each parameter into normal and extreme values. The color assignment, according to the quadrant gates, is demonstrated in the scatter plots of FA mean intensity and axial ratio as a function of FA area in control reporter cells (Fig. 3d and e, respectively). This quadrant-based coloring depicts large vs. small, elongated vs. round, and bright vs. less intense FA, where large FA with high mean intensity (red cross, Fig. 3b) and large FA with elongated shape (red cross, Fig. 3c) constitute a small subpopulation located mainly at the cell periphery. Since these FA subpopulations can be correlated with different adhesion types [e.g., small and round focal complexes (FX) or elongated fibrillar adhesions (FB)], we expect such an analysis to supply clues to physiological responses induced by the extracts. For example, contraction of actin bundles increases the size and elongation of FA, and often induces loss of FX and FB.

3.3. Automated scoring of changes in FA

The automated analysis was applied, based on a comparison between the accumulated histograms and scatter plots of FA parameters from each treated well with the respective parameters in the control wells, to identify the effective extracts (see Section 2). We found the best scores, in terms of contrasting histograms of affected vs. unaffected wells, based on Kolmogorov–Smirnov test (KSsa, see Supplementary Methods online), comparison of 90th percentile values, and quadrants of area vs. mean intensity or vs. axial ratio. KSsa best integrates changes throughout the tested histograms, whereas the 90th percentile and quadrants depict effects on the distribution tails. We found these statistical scores to be complementary. By applying all scores to mark the most severely affected wells, we decreased the risk of missing subtle effects. The output of the automated analysis for each parameter and every statistical method are plate matrices in which each well is painted according to its color-coded score (Fig. 4). For the 90th percentile analysis, red represents values that are larger than the 90th percentile of the control and blue represents lower values. Green indicates that no significant variation from the control was detected. For the KSsa analysis, red indicates large deviation from the control histogram; however, the use of absolute values to accumulate the difference between the two histograms causes loss of the change's "directionality" (one-sided test). In the quadrant analysis, the fraction

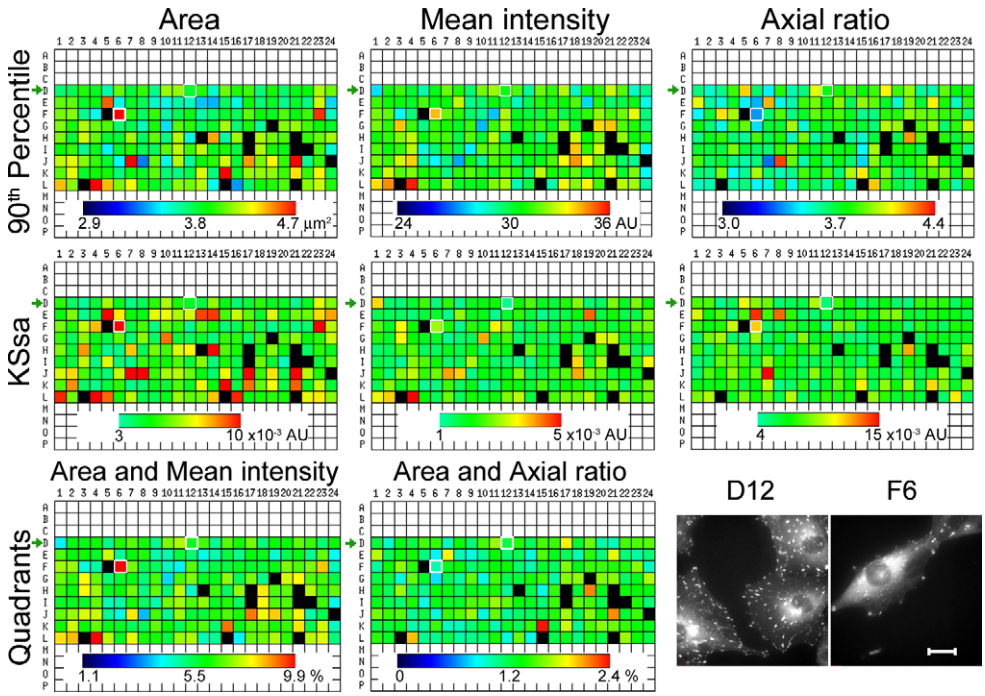

Fig. 4. Whole plate analysis. The FA parameter distributions in each well within the plate were compared to control (row D, green arrows) as described in Section 2. FA area, mean intensity and axial ratio were compared using the 90th percentile value (top row), KSsa (middle row) and fraction of FA in the 4th quadrants (high mean intensity or axial ratio and large area, (bottom row)). Wells with less then 12% cell coverage were considered unsuitable for statistical analysis, and marked black. Odd rows include cells treated with 100 μg/ml of extract and even rows with 10 μg/ml. Images of control (from well D12) and of a treated cell (from well F6) are shown at the lower left corner. The corresponding wells are outlined in white squares in the plate GUI. The treated cells have small amount of large, bright and rounded FA, which are located mainly at the cell periphery. Scale bar: 20 μm.

of FA with extreme parameters (e.g., large and elongated or large and bright) was calculated from the total FA population, using green to indicate the fraction in control wells and red and blue for larger and smaller fractions, respectively. As expected, only some affected wells got high ranks for all parameters, while others were "highlighted" differently for each parameter. Note that every pair of columns in each plate is treated with the same extract at 100 μg/ml and at 10 μg/ml, revealing different effects at the two concentrations. The plate-analysis software also produces a list of wells ordered by their score, and displays the corresponding well montages for visual monitoring of the automated scoring process.

Massive loss of cells in some wells (due to toxicity or anti-adhesive activity of the extract) resulted in a highly variable phenotype, reflecting large statistical error due to the small number of segmented objects. We therefore overwrote, in black, the color of wells with a low percentage of "cell coverage" (<12%, compared to >60% in control wells; see Fig. 4).

To evaluate the correlation between the different statistical scoring methods used, we plotted the ranks of the top 20 scores in a typical plate, according to KSsa and 90th percentiles for FA area, mean intensity and axial ratio (Fig. 5). We found that the two methods yield highly correlated scores for FA area but a low correlation between scores for FA mean intensity and FA axial ratio. FA size is, therefore, a parameter that is typically affected for most FA in treated cells, whereas intensity and axial ratio are parameters that may change in only a fraction of the FA population.

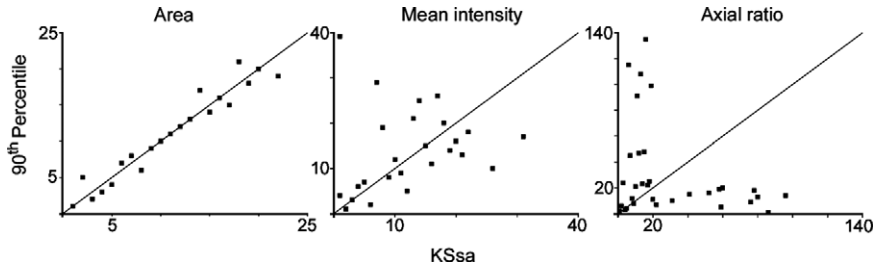

Fig. 5. Comparison of statistical scoring by 90th percentiles and by KSsa. The 20 wells with the highest scores for the statistical analysis of FA area, mean intensity and axial ratio, are plotted according to their two ranks. Correlation between the ranks according to the two statistical methods is high for area, lower for mean intensity, and totally absent for axial ratio. The line in each plot represents equal ranks.

In this screen, approximately 1% of the extracts tested using the automated analysis showed strong effects on FA. About 5% showed mild effects and ca. 15% induced cell detachment or loss at the working dilutions (Table 2). The five most prominent phenotypes obtained in this screen are shown in Fig. 6a and in Table 2.

3.4. Interactive analysis of the cellular effects induced by library components

The automatic processing described here defines and quantifies FA structures within the image, as well as areas within the image covered by cells. The current software does not define individual cells and thus cannot quantify the various parameters per cell. In addition, information about the organization of FA in the context of the cell cannot be defined. We thus further analyzed images of "flagged hits" by manually outlining individual cells and considering only the enclosed FA, yielding a better characterization of the phenotypes found by the automated screen. The additional parameters calculated following cell outlining were distance from the cell edge normalized to cell radius (NDE), orientation of FA with respect to the cell center, and the number of FA per cell (Table 1). The mean values per cell of representative parameters, obtained by the interactive analysis, are provided in Fig. 6b. The plot of number of FA per cell demonstrates the dramatic reduction in this parameter following treatment with BGYP2-2, BGYP2-3 and BGYP2-4. The fraction of FA larger than 3.33 μm^2 (90th percentile of FA area value in control cells) shows the significant change from the control for BGYP2-4. Using quadrant-gating analysis, the fraction of large FA with high intensity was significantly larger for BGYP2-10 than for all others, and for BGYP2-6 the quadrant of large and elongated FA increased, distinguishing the elongation phenotype. Finally, quadrant gating of NDE and FA area demonstrated the enhancement of the peripheral population of large FA for BGYP-10 and BGYP-6. Although all of these phenotypes were highlighted by the automated analysis, reference to the individual cells allowed differenti-

Table 2
Focal adhesion affecting extracts from the NCHTS[a] natural-extracts library

Extract	Source	Effect at 100 μg/ml[b]	Minimal effective concentration	Total number of extracts with similar phenotype[c]
BGYP2-10	Plant *Crataegus*	Loss of adhesion at the cell center	100 μg/ml	5
BGYP2-6	Fungus *Aspergillus*	FA elongation at the cell periphery	100 μg/ml	1
BGYP2-4	Tree *Pinus*	Reduction in FA paxillin signal intensity	100 μg/ml	4
BGYP2-3	Sponge *Jaspis*	Cytoskeletal disruption	10 ng/ml	5
BGYP2-2	Sponge *Clionid affiliation*	Cytoskeletal disruption	10 μg/ml	5
BGYP2-17	Sponge *Theonella*	Cell detachment or loss	100 μg/ml	333

[a] http://www.tau.ac.il/~nchts.
[b] Images are shown in Fig. 6a.
[c] For images of all screened extracts with strong effect on focal adhesions see http://www.weizmann.ac.il/mcb/Geiger/Screening.html.

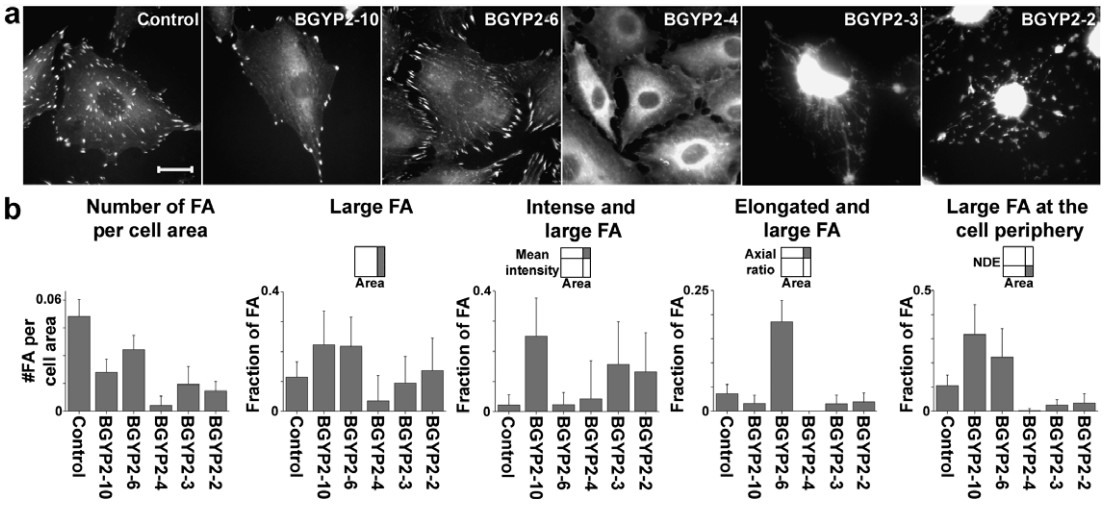

Fig. 6. FA perturbation phenotypes and their quantification. (a) Representative images of control and five treated wells showing different phenotypic effects (see text and Table 2). Scale bar: 20 μm. (b) Fraction of FA sub-populations, defined by one- and two-parameter gates, for the control and the five phenotypes in (a). The number of FA with parameter values within the ranges defined by the gates were calculated as a fraction from the total population of FA in each cell. The mean and standard-deviation for 10 cells in each phenotype are presented in the bar plots. The gates, indicated schematically above each bar plot, are: area >3.33 μm^2, mean intensity >32, axial ratio >2.9 and NDE <0.1. Gate values were determined from 90th percentiles for the control.

ating between the various patterns of cell phenotypic responses of FA to the different drugs.

3.5. Dose- and time-dependent effects of the extracts on FA

The screen scored an extract marked BGYP2-3 as one of the most potent sources for FA modulation. This extract is obtained from the marine sponge, *Jaspis* sp., which has been a source of biologically active compounds in the past (Kobayashi et al., 1993; Zampella et al., 2000). A dose-dependence experiment (Fig. 7a), carried by the same procedures of the large screen, demonstrated that at 100 μg/ml, it causes severe cytoskeletal perturbation and completely destroys FA structures. Additional dilution of the extract (1 μg/ml) induced the appearance of doublets of small FA, and at further dilution (10 ng/ml), thick stress fibers with paxillin localization were observed (seen also by phalloidin staining, not shown). At concentrations below 10 ng/ml, no effects could be detected. The concentration dependence is depicted by KSsa scoring of FA area (Fig. 7b).

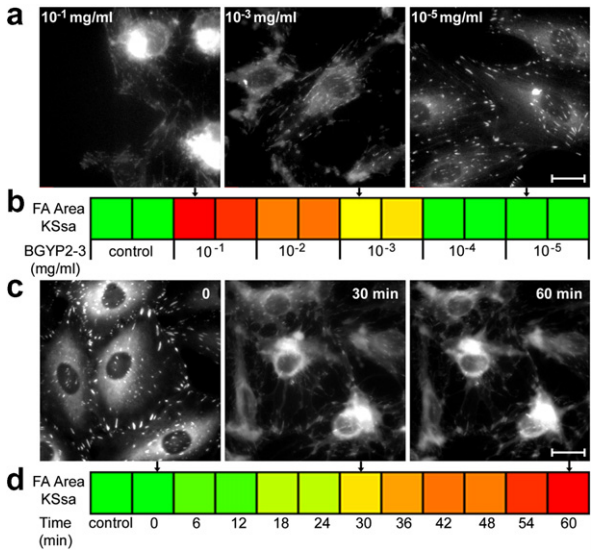

Fig. 7. Dose-dependent and time-lapse experiments and their KSsa analysis. (a) Dose-dependent effect of the crude extract BGYP2-3 (containing Jaspamide). Typical images of cells treated with extract concentration of 100 μg/ml, show massive cell damage, 1 μg/ml show doublets of small FA and 10 ng/ml show large stress fibers (displayed by phalloidin staining, not shown). Scale bar: 20 μm. (b) The quantitative analysis of the data based on FA area and KSsa comparison to control. The colors mark the scores; red denotes a large deviation from control and green indicates similarity to control. Each dilution was tested in duplicates. (c) Time dependence of the effect of BGYP2-3 (10 μg/ml) on FA structure. Images were acquired for 1 h at 6 min intervals. Before treatment, the cells were spread. After addition of the extract cells started to retract, leading to reduction in FA number and size. After 1 h of treatment all cells were fully shrunk and only traces of a few small FA are left. No recovery was observed following removal of the extract. Scale bar: 20 μm. (d) Quantitative analysis of the data from time-lapse movie, using KSsa for FA area, demonstrates the increasing deviation from control with time.

Time-lapse movies were carried by the automated system cycling between wells with different treatments and acquiring multiple movies simultaneously. Cells treated with BGYP2-3 at 10 μg/ml (Fig. 7c) showed fast cytoplasmic retraction starting after 6 min of treatment, leading to a reduction in FA number and size. After 1 h of treatment, all cells were fully affected and only traces of small FA were left. No recovery was observed following extract washout from the medium. These time-dependent effects were quantified by KSsa scoring of FA area (Fig. 7d).

3.6. Isolation and characterization of the specific component affecting FA structure in the BGYP2-3 extract

To purify the active compound from the crude extract of BGYP2-3, we conducted an iterative process of fractionation and parallel screening. Each fraction was tested at up to 11 dilutions for its effect on FA integrity. The number of samples tested for each fractionation stage varied from 5 to 16. The analysis of the effect of each fraction using KSsa scoring of FA area reveals the most effective fraction by means of lower effective concentration (see Supplementary Fig. 1 online). This fraction was subjected to further purification. The purification process (see Section 2) was followed by identification of the structural signatures using 1D and 2D NMR and MS spectra. These analyses indicated that the active compound is jaspamide. The cytoskeletal disruption, as well as the formation of FA doublets and thick stress fibers following treatment with BGYP2-3 extract is in line with the notion that jaspamide (jasplakinolide) binds to and stabilizes F-actin (Bubb et al., 1994; Bubb et al., 2000; Scott et al., 1988). The purification of jaspamide, a known cytoskeletal-modulating compound, achieved here based on its effect on FA morphology, serves as a proof of principle for the methodology. Currently, additional extracts are being iteratively fractionated and tested for FA effects with the aim of identifying additional cytoskeleton-perturbing compounds.

4. Discussion

The development of the automated HTR microscopy platform described here was motivated by the need to perform comprehensive cell-based screens, yet harvest detailed, high-resolution information from each sample. This approach has a particular value when the cellular structures examined have dimensions ranging from a fraction of a μm to a few μm, and when the investigated treatment is expected to introduce subtle differences in these structures. The success of such screens over existing approaches depends on three major factors: the quality of the library, the choice of reporter cell and the performance of the microscopy platform. In the development of the HTR microscope, two further technological barriers had to be overcome, namely fast and automated high-resolution focusing, and online interpretation and quantitative analysis of changes in cell images. First, we briefly discuss

the natural-extracts library and the cells used in this screen, and then we address, in detail, the features of the automated microscope and the image-processing strategy.

The natural-extracts library used here was derived from a wide variety of marine and terrestrial organisms. Such extracts are mixtures of molecules, and thus the identification of specific bioactive compounds requires a purification process, as demonstrated here for the *Jaspis* sample. The monitoring of fractions and their dose- and time-dependent effects requires multiple-well experiments, which benefit from utilization of the HTR platform.

The successful discovery of new bioactive molecules also depends on the properties of the reporter cells used for testing the compound library. The nature of the tested cells is determined by the specific objectives of the screen; nevertheless, there are considerations that are applicable to cell-based screens in general. These include the use of cells with uniform morphology and plating density, intense labeling which enables short exposures, and a high signal-to-noise ratio for reliable image interpretation.

The major achievement reported here is the integration of the screening microscopy platform. We describe the substantial steps taken towards addressing the two major barriers in HTR microscopy: fast autofocusing and image analysis and interpretation. The laser-based AutoFocus system allows very fast acquisition of images using a 60×/0.9 NA objective at 0.3-μm resolution. The system achieves a throughput of 3×10^3 images per hour, or a couple of hours for a 384-well plate, with 25 images per well, which yields a sufficiently large sample size of about 50 cells for meaningful statistical testing. To achieve a comparable rate of data processing for hit identification, we developed an automated image-analysis pipeline that scores the differences between treated cells and controls, and "flags" wells displaying conspicuous effects. Last we employ the multi-well format, the automated acquisition and the quantitative analysis in the identification of the active fraction in positive extracts.

We applied segmentation-based algorithms to characterize treatment effects, based on morphological and fluorescence-intensity multi-parametric quantifiers for the segmented objects. In addition, segmentation of cell-covered area indicated cell shrinkage and cell loss, and provided normalization factor. Despite the variability between individual cells and individual control wells, we show that the accumulated statistical data can detect subtle but meaningful differences between control and perturbed cells. The quantitative multi-parametric information defined by the segmented subcellular structures is extremely important for further characterization of the hits.

Segmentation algorithms are image-specific and susceptible to artifacts when applied to complex pictures such as high-resolution cell images. However, tailoring the analysis to the specific patterns by selecting multi-parameter ranges for the segmented object while excluding outliers resulted in reliable scores. To supervise and monitor the computerized analysis, we provide convenient tools for visualization of the acquired image data and the analysis steps. Further software developments call for the application of additional algorithms working within the multi-dimensional parameter space created by the analysis (e.g., principle component analysis (Tanaka et al., 2005), multi-dimensional distances, pattern correlations and clusters (Perlman et al., 2004), and machine learning methods (Hu and Murphy, 2004)). Improvement of the automated analysis will include recognition of cell outline for better identification of individual cells. Such analysis can provide information on cell numbers and dimensions, number of FA per cell and their intracellular localization, features that were quantified by us interactively, and were found to be characteristic phenotypes (e.g., extract BGYP2-10, Fig. 6a). An automated outlining of individual cells yielding reliable information for both single cells and confluent islands is currently under development.

In summary, we present a novel screening platform, based on HTR microscopy, to search for fine alterations in subcellular structures. This platform was used here to quantify structural features of FA, but the approach can be tailored to quantify a wide variety of subcellular structures. Indeed, the same screening platform, with only minor modifications, is currently being used for multiple cell-based screening projects, including a cell-migration screen, a screen of FA perturbations by siRNA or by chemical compounds, and *Drosophila* genome-wide RNAi screen.

Acknowledgments

We thank Dr. Irena Lavelin for the paxillin-YFP pBabe plasmid and for help in establishing the reporter cell line, and Prof. Edna Schechtman for consulting on statistical methods. The research reported here is supported by grants from the Kahn Fund for Systems Biology at the Weizmann Institute of Science (Z.K.), the NIGMS, National Institutes of Health Cell Migration Consortium Grant U54 GM64346 (B.G.), the Israel Science Foundation (B.G.), Yad Abraham Center for Cancer Diagnosis and Therapy, and the Clore Center for Biological Physics (Z.K.). B.G. holds the E. Neter chair in Cell and Tumor Biology, Z.K. is the Israel Pollak Professor of Biophysics.

Appendix A. Supplementary data

Supplementary data associated with this article can be found, in the online version, at doi:10.1016/j.jsb.2006.12.013.

References

Abraham, V., Taylor, D., Haskins, J., 2004. High content screening applied to large-scale cell biology. Trends Biotech. 22, 15–22.

Arrasate, M., Finkbeiner, S., 2005. Automated microscope system for determining factors that predict neuronal fate. Proc. Natl. Acad. Sci. USA 102, 3840–3845.

Brown, M.C., Turner, C.E., 2004. Paxillin: adapting to change. Physiol. Rev. 84, 1315–1339.

Brownlee, K., 1965. Statistical Theory and Methodology in Science and Engineering, second ed. John Wiley & Sons, New York.

Bubb, M.R., Senderowicz, A.M., Sausville, E.A., Duncan, K.L., Korn, E.D., 1994. Jasplakinolide, a cytotoxic natural product, induces actin polymerization and competitively inhibits the binding of phalloidin to F-actin. J. Biol. Chem. 269, 14869–14871.

Bubb, M.R., Spector, I., Beyer, B.B., Fosen, K.M., 2000. Effects of jasplakinolide on the kinetics of actin polymerization. An explanation for certain in vivo observations. J. Biol. Chem. 275, 5163–5170.

Butcher, E.C., 2005. Can cell systems biology rescue drug discovery? Nat. Rev. Drug Discov. 4, 461–467.

Clemons, P.A., 2004. Complex phenotypic assays in high-throughput screening. Curr. Opin. Chem. Biol. 8, 334–338.

Conrad, C., Erfle, H., Warnat, P., Daigle, N., Lorch, T., Ellenberg, J., Pepperkok, R., Eils, R., 2004. Automatic identification of subcellular phenotypes on human cell arrays. Genome Res. 14, 1130–1136.

Giuliano, K.A., Haskins, J.R., Taylor, D.L., 2003. Advances in high content screening for drug discovery. Assay Drug Dev. Technol. 1, 565–577.

Hu, Y., Murphy, R.F., 2004. Automated interpretation of subcellular patterns from immunofluorescence microscopy. J. Immunol. Methods 290, 93–105.

Kobayashi, J., Murata, O., Shigemori, H., 1993. Jaspisamides A–C, new cytotoxic macrolides from the Okinawan sponge *Jaspis* sp. J. Nat. Prod. 56, 787–791.

Koehn, F.E., Carter, G.T., 2005. The evolving role of natural products in drug discovery. Nat. Rev. Drug Discov. 4, 206–220.

Liebel, U., Starkuviene, V., Erfle, H., Simpson, J.C., Poustka, A., Wiemann, S., Pepperkok, R., 2003. A microscope-based screening platform for large-scale functional protein analysis in intact cells. FEBS Lett. 554, 394–398.

Liron, Y., Paran, Y., Zatorsky, N.G., Geiger, B., Kam, Z., 2006. Laser autofocusing system for high-resolution cell biological imaging. J. Microsc. 221, 145–151.

Mitchison, T.J., 2005. Small-molecule screening and profiling by using automated microscopy. Chembiochem 6, 33–39.

Murphy, R.F., 2004. Automated interpretation of protein subcellular location patterns: implications for early cancer detection and assessment. Ann. N. Y. Acad. Sci. 1020, 124–131.

Paran, Y., Lavelin, I., Naffar-Abu-Amara, S., Winograd-Katz, S., Liron, Y., Geiger, B., Kam, Z., 2006. Development and application of automatic high-resolution light-microscopy for cell-based screens. Meth. Enzymol. 414, 228–247.

Perlman, Z.E., Mitchison, T.J., Mayer, T.U., 2005. High-content screening and profiling of drug activity in an automated centrosome-duplication assay. Chembiochem 6, 145–151.

Perlman, Z.E., Slack, M.D., Feng, Y., Mitchison, T.J., Wu, L.F., Altschuler, S.J., 2004. Multidimensional drug profiling by automated microscopy. Science 306, 1194–1198.

Peterson, J.R., Mitchison, T.J., 2002. Small molecules, big impact: a history of chemical inhibitors and the cytoskeleton. Chem. Biol. 9, 1275–1285.

Press, W., Flannery, B., Teukolsky, S., Vetterling, W., 1986. Numerical Recipes. Cambridge University Press, Cambridge.

Scott, V.R., Boehme, R., Matthews, T.R., 1988. New class of antifungal agents: jasplakinolide, a cyclodepsipeptide from the marine sponge, *Jaspis* species. Antimicrob. Agents Chemother. 32, 1154–1157.

Smith, C., Eisenstein, M., 2005. Automated imaging: data as far as the eye can see. Nat. Methods 2, 547–555.

Tanaka, M., Bateman, R., Rauh, D., Vaisberg, E., Ramachandani, S., Zhang, C., Hansen, K.C., Burlingame, A.L., Trautman, J.K., Shokat, K.M., Adams, C.L., 2005. An unbiased cell morphology-based screen for new, biologically active small molecules. PLoS Biol. 3, e128.

Yarrow, J.C., Feng, Y., Perlman, Z.E., Kirchhausen, T., Mitchison, T.J., 2003. Phenotypic screening of small molecule libraries by high throughput cell imaging. Comb. Chem. High Throughput Screen 6, 279–286.

Zamir, E., Katz, B.Z., Aota, S., Yamada, K.M., Geiger, B., Kam, Z., 1999. Molecular diversity of cell-matrix adhesions. J. Cell Sci. 112 (Pt. 11), 1655–1669.

Zampella, A., D'Auria, M.V., Debitus, C., Menou, J.L., 2000. New isomalabaricane derivatives from a new species of *Jaspis* sponge collected at the Vanuatu islands. J. Nat. Prod. 63, 943–946.

Zhao, T., Velliste, M., Boland, M.V., Murphy, R.F., 2005. Object type recognition for automated analysis of protein subcellular location. IEEE Trans. Image Process 14, 1351–1359.

Zhou, X., Cao, X., Perlman, Z., Wong, S.T., 2006. A computerized cellular imaging system for high content analysis in Monastrol suppressor screens. J. Biomed. Inform. 39, 115–125.